Modelling of current distribution in Nb_3Sn multifilamentary strands subjected to bending

2012 Supercond. Sci. Technol. 25 054003

(http://iopscience.iop.org/0953-2048/25/5/054003)

Supercond. Sci. Technol. **25** (2012) 054003 (9pp) doi:10.1088/0953-2048/25/5/054003

Modelling of current distribution in Nb_3Sn multifilamentary strands subjected to bending

Y Miyoshi, C Zhou, E P A van Lanen, M M J Dhallé and A Nijhuis

University of Twente, Energy, Materials and Systems, Faculty of Science and Technology, 7522nd Enschede, The Netherlands

E-mail: A.Nijhuis@utwente.nl

Received 4 December 2011, in final form 10 February 2012
Published 23 April 2012
Online at stacks.iop.org/SUST/25/054003

Abstract

In Nb_3Sn cable-in-conduit conductors (CICCs), strands follow complex trajectories that result in a periodic bending strain acting on the strands upon electromagnetic loading and thermal contraction. Such a periodic bending strain leads to degradation of the overall transport performance of a CICC. Aiming for a better understanding and quantitative correlation between strand degradation and CICC test results, a detailed strand model is essential in combination with accurate intra-strand resistance data, the spatial filament strain distribution, and the associated filament crack distribution. Our novel numerical strand model is a 3D network of resistors including superconducting filaments, normal matrix elements, and an outer stabilizing shell or inner core. Along the strand length, matrix elements have Ohmic resistance, there is a filament-to-matrix contact resistance (R_{fm}) between filaments and matrix elements, while superconducting filaments have a power-law voltage–current (VI) characteristic with critical current (I_c) and an n-value described by the ITER Nb_3Sn strain scaling law based on measured strand data. The model simulates the VI characteristic in a periodic bending experiment and provides the associated spatial potential distribution. The VI characteristics representing the low- and high-resistivity limits (LRL and HRL) are identified for periodic and uniform axial bending. The voltage level for the current transfer regime depends on the strand internal resistivities, i.e. the filament-to-matrix contact and the matrix resistivity, the twist pitch and the bending wavelength.

The simulation results show good agreement against I_c degradation, as experimentally measured by the TARSIS facility, versus the assessed peak bending strain. In addition we discuss different methods for determining the applied peak bending strain. The model provides a basis to find a practical relationship between a strand's VI characteristic and the periodic bending strain, as well as a mapping of well-characterized strand performance to that of a full-size CICC.

(Some figures may appear in colour only in the online journal)

1. Introduction

The transport properties of Nb_3Sn strand under periodic bending strain anticipated from thermal and electromagnetic loads in an ITER cable-in-conduit conductor (CICC) has been studied by both experimental [1–4] and modelling work [5–9]. The strain sensitive criticalities and the brittle nature of Nb_3Sn result in degradation of I_c due to an applied periodic strain, and in the worst case lead to filament fracture. The ultimate goal of such work is to find a mapping of well-characterized strand performance to that of a full-size CICC, as well as to explain the origin of continuing degradation with cyclic electromagnetic and thermo-mechanical loading found in short sample tests performed at SULTAN (SUpraLeiter

Test ANlage). At present, there is no definitive method to predict CICC performance from strand characteristics. The motivation of the modelling work presented here is to find a relationship between the strand *VI* characteristic and periodic bending strain, which will eventually be used in a full-size strand-level-based electromagnetic CICC model [10]. The periodic bending strain pattern can be obtained from a detailed mechanical cable model, providing a strain map of all individual strands [11].

In the past, the transport of inhomogeneous NbTi multifilamentary strands has been modelled by considering a distribution of I_c due to filament inhomogeneities [12] across the strand transverse cross section [13] and along the strand length [14]. Likewise, when a Nb_3Sn strand is bent, a strain distribution, and consequently an I_c distribution, is introduced across the strand transverse cross section and along the strand length. The present day modelling efforts for Nb_3Sn strand take the pioneering work of Ekin [15] as a reference, in which analytical formulae for the two limiting cases of strand I_c under uniform bending are given. Often, the two limits are referred to as the high-resistivity limit (HRL) and the low-resistivity limit (LRL). In the HRL, the strand internal resistivity inhibits current sharing among differently strained filaments, while in the LRL all filaments are involved in current sharing. The strand behaviour between the two limits can be calculated numerically [9] or empirically [7, 16].

The precursor of the present numerical strand model was developed in order to simulate the influence of filament fracture on the *VI* characteristic [17]. The basic structure of the model considers the current transfer effect between individual filaments in a metal matrix, hence, the system to be solved is a network of superconducting filaments and metal matrix elements [18].

Employing the same model structure, a spatial distribution of the I_c for individual filaments is implemented to account for the applied periodic bending strain. The filament strain under periodic bending may be calculated from the shape of periodic strand bending, as has previously been done for calculating the peak bending strain in TARSIS (Test ARrangement for Strain Influence on Strands) experiments [1–3]. In this model, however, we utilize the mechanical model of a strand based on the finite-element model (FEM) [11] to map the spatial distribution of individual filament strains. The peak bending strain as determined for the TARSIS bending deflection in our earlier papers was based on the simplified relationship presented in [1, 2], which leads to a difference of about 20%. However, the strand is still modelled as a homogeneous medium and further development of the mechanical model is foreseen to exclude influence from the detailed strand inner structure and the plasticity of the materials involved. From the filament strain map, the local filament I_c is assigned according to the ITER I_c scaling function [19].

The new strand model simulates current transfer effects between filaments with different I_c. The resultant *VI* characteristic is interpreted by the voltage dependent transition between two limiting cases, which are analogous to the HRL and LRL of the uniform bending case. We present the basic model structure and behaviour, its dependence on simulation parameters such as the input resistive parameters and the bending periodicity with respect to the strand twist pitch, and our interpretations in terms of limiting cases. Furthermore, the influence of the location of the potential taps is discussed and the model predictions are compared with TARSIS experimental data from an internal tin strand and one restacked-rod process (RRP) strand.

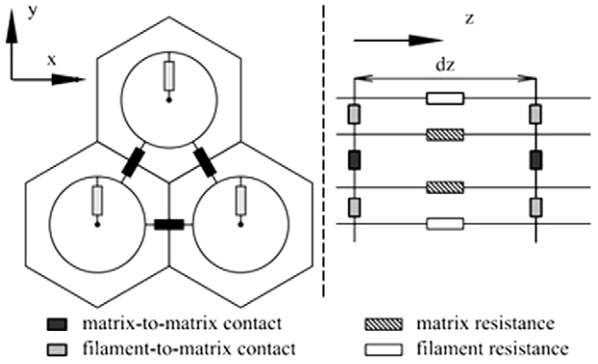

Figure 1. Schematic description of the model structure: transverse (left) and longitudinal (right) cross sections.

2. Network model

The model consists of a three-dimensional resistive network of superconducting filaments and normal matrix elements arranged in a regular pattern. The first step of this modelling effort is to investigate the experimentally measured results of Nb_3Sn strands under periodic bending; the strands concerned have an ordered structure, which is typically hexagonal. Hence, in the transverse direction, the matrix is divided in hexagonal surfaces, each of which encloses one superconducting filament (figure 1).

For simplicity, it is assumed that the potential of each matrix element is equal everywhere around the filament. This makes it possible to represent the contact resistance between the matrix element and the filament by a single resistor. The matrix elements are connected by a resistor only if they share a border. This is represented in figure 1 by the black resistors. In the longitudinal direction, the matrix elements are connected with each other by a resistor, whereas the resistivity of the superconducting filaments is determined by a power-law relationship between the current and voltage. For such a network, we solve the well-known current transfer problem at a metal/superconductor interface [18]. The model solves numerically the following equations,

$$\frac{\mathrm{d}^2 i_{\mathrm{m},p,q}}{\mathrm{d}z^2} = \frac{\pi d_\mathrm{f}}{R_\mathrm{fm}}\left(R_{\mathrm{m}z} i_{\mathrm{m},p,q} - E_\mathrm{c}\left(\frac{i_{\mathrm{f},p,q}}{i_{\mathrm{c},p,q}}\right)^{n_{p,q}}\right) + \sum_{k=1}^{N_\mathrm{f}} \frac{R_{\mathrm{m}z}}{\rho_{\mathrm{m}y,q,k}}(i_{\mathrm{m},p,q} - i_{\mathrm{m},p,k}) \quad (1)$$

$$\frac{\mathrm{d}^2 i_{\mathrm{f},p,q}}{\mathrm{d}z^2} = \frac{\pi d_\mathrm{f}}{R_\mathrm{fm}}\left(E_\mathrm{c}\left(\frac{i_{\mathrm{f},p,q}}{i_{\mathrm{c},p,q}}\right)^{n_{p,q}} - R_{\mathrm{m}z} i_{\mathrm{m},p,q}\right), \quad (2)$$

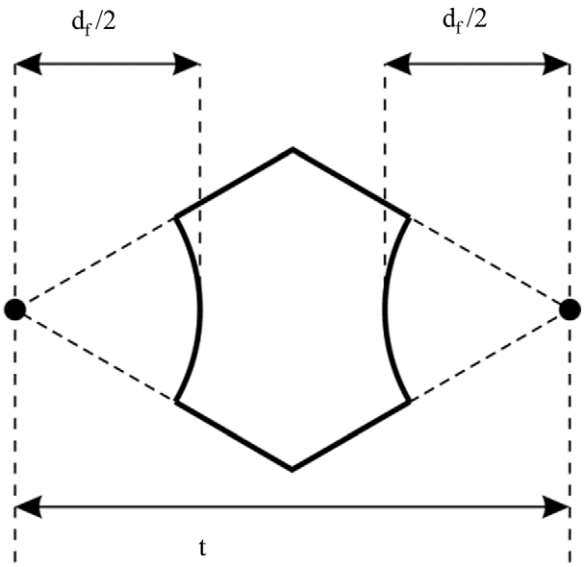

Figure 2. A schematic representation of the conduction channel in the matrix between two filaments.

where the matrix current i_m and the filament current i_f at pth z-coordinate and qth filament of the total N_f filaments are involved. Note that the sum in (1) does not involve all the matrix elements, only those that are in direct contact. The input resistive parameters are R_{fm} in Ω m^2 for the filament-to-matrix contact resistance and the matrix resistivity ρ_m is in Ω m. They are experimentally measured values [20–22]. The longitudinal matrix resistance R_{mz} depends on ρ_m by dividing it by the matrix element area A_m. The latter can be determined from the filament diameter d_f and distance t between the filaments

$$A_m = \sqrt{3}t - \pi d_f^2. \tag{3}$$

In a similar way, the transverse resistance term ρ_{my} depends on ρ_m and the dimension of the conduction channel between matrix elements. Its value is approximated by (figure 2)

$$\rho_{my} = \rho_m \frac{t}{w} = \rho_m \left(1 - \frac{d_f}{t}\right)\sqrt{3}. \tag{4}$$

Verification with equivalent models constructed in commercially available finite-element software has demonstrated that this approximation is acceptable for our purpose. Each filament section is assigned its own I_c and n-value. A detailed derivation of the equations can be found in [17].

The 3D grid points are constructed for a strand with a transverse cross section consisting of a network of hexagonal cells, as discussed above. An example of a strand cross section is shown in figure 3. The cross section has two types of hexagonal matrix element. The inner region corresponds to the filamentary region of the strand. Here, the matrix elements contain superconducting filaments. The cells in the region outside do not contain any superconducting filaments and the resistivity of Cu is used to represent the stabilizing shell.

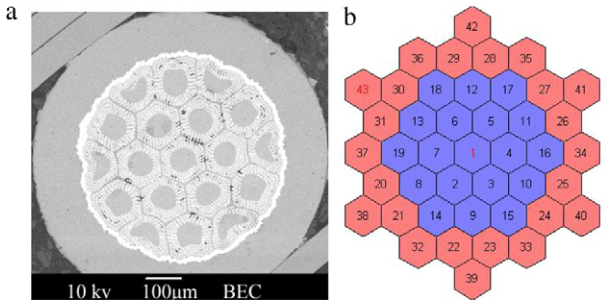

Figure 3. An example of a strand cross section. (a) SEM micrograph of an OST1 strand [23]. (b) Model cross section for an OST1 strand. The inner region (elements 1–19) is the filamentary region and the region outside (elements 20–43) is the Cu shell.

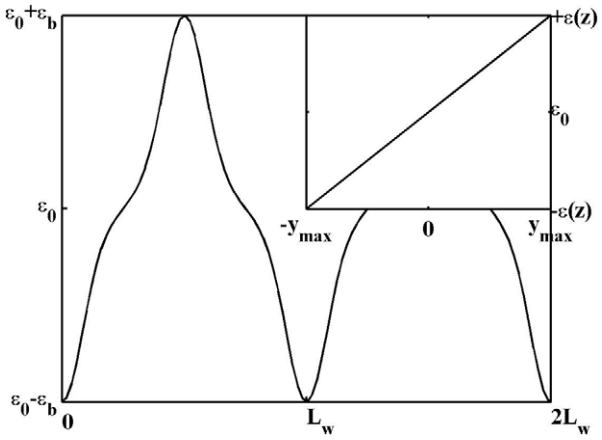

Figure 4. Periodic peak bending strain in the z-coordinate, where L_w is the bending period. In transverse direction, the strain is distributed linearly with the y-coordinate, where $y = 0$ is the neutral axis of the strand (inset).

For periodic bending, we assign the I_c and n-value of individual filaments at each z-coordinate as periodic functions. In order to evaluate the local I_c values, a strain map is obtained from the FEM calculation presented in [11], for a homogeneous beam under transverse loading from periodically alternating bulges, as in the case of TARSIS measurement. The shift of the neutral axis due to plastic deformation and filament fractures [24] has not been taken into account. When the amplitude of periodic bending is small, the peak bending strain along the strand can be approximated well by a sine series and we assume that the strain is distributed linearly in the transverse direction (figure 4). To each filament segment, the strain is mapped according to its corresponding y-coordinate, that is, the strain map of a filament is a function of both periodic bending strain and strand twisting. Using the strain map, the corresponding I_c and n-value are evaluated from the measured strand I_c strain dependence [25]. We assume that all filaments are identical in their properties and only consider applied strain as a variable.

To summarize, the model solves the current transfer problem between filaments and matrix elements where the transport properties of filaments vary for each filament in

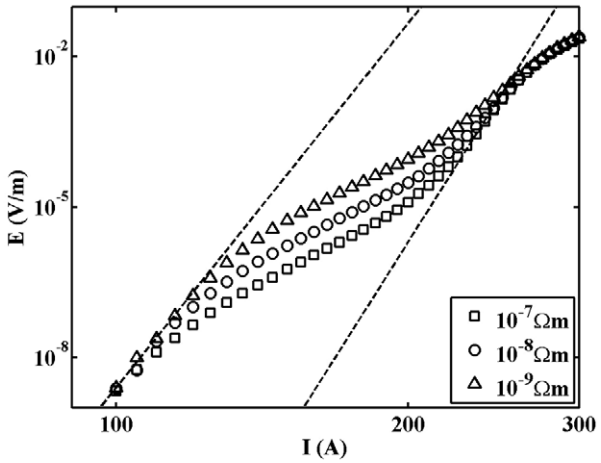

Figure 5. *E–I* plots simulated for three different input values of ρ_m (symbols). The vertical dashed lines are the limiting cases of E_{cs} (at higher current) and E_{nf} (at lower current).

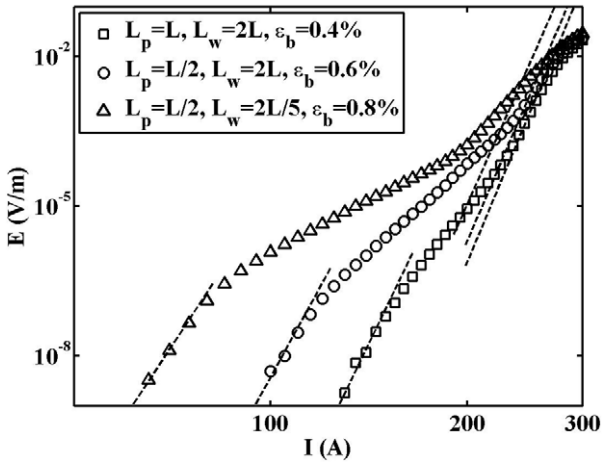

Figure 6. Simulated *E–I* plots (symbols) for $\rho_m = 1 \times 10^{-8}$ Ω m with three different combinations of the bending wavelength, twist pitch, and peak bending strain. Vertical dashed lines are E_{cs} and E_{nf} for each curve.

each segment according to the applied strain profile. The input parameters to the model are the measured strand dimensions, d_f and t, the measured resistive parameters, R_{fm} and ρ_m, and finally the filament strain map calculated from the finite-element mechanical strand model.

3. Model simulations and analytical limits

The model behaviour is demonstrated for the case of 31 filaments and 24 outer Cu shell elements. The strain distribution is simulated for the simple case of one bending period over one strand twist pitch length (L_p). The strand length in the simulation is 30 mm and we sample the voltage drop over 25 mm, equidistant from the middle. The I_c and n-value are calculated for a peak bending strain 0.6% and a thermal pre-strain −0.24%, using the measured strand scaling relationship for an ITER TF-type bronze strand [3]. The contact resistance R_{fm} is 1×10^{-15} Ω m^2, which is a typical measured value [20, 21]. Three different values for ρ_m are chosen to show the effect of the strand matrix resistivity. The Cu shell resistivity is kept constant at 7×10^{-10} Ω m. The strand size parameters t and d_f are arbitrarily chosen to be 90 and 70 μm, respectively. In the three simulated cases, the electric field versus current (EI) curves encounter two limits at high and low voltage and a transition in-between (figure 5).

In the multifilamentary superconductor with filaments having different I_c, there is a balance between two possible resistive paths; one path along the superconducting filament with power-law resistance, and the Ohmic path in the matrix channel that connects filaments. Therefore, in the three simulated cases, the limiting behaviours are the same, as they are determined by the I_c distribution, but the transition voltage is different, as it is determined by the matrix resistivity.

We interpret the limiting EI at high voltage as the case where the potential difference along the strand length is sufficient to involve all filaments in current sharing such that the entire strand behaviour is described by the average property of all filaments. Hence, the limiting EI at high voltage is given by the mean I_c at each strand segment dz. By integrating along the strand length,

$$E_{cs} = \frac{\int E_c \left(\frac{I}{I_{cm}(z)}\right)^{n_m(z)} \mathrm{d}z}{\int \mathrm{d}z}, \tag{5}$$

the current sharing limit E_{cs} is given by the strand mean values of I_c (I_{cm}) and n-value (n_m) at each z-coordinate. This expression is analogous to Ekin's LRL, apart from the variation along the strand length.

At low voltage, we may consider that the individual filaments preferentially carry current without extensive current sharing with their nearest neighbours. In the limiting case, where no current is shared, the limiting electric field E_{nf} is given by a summation of single filament voltages,

$$E_{nf} = \frac{\int \sum_q^{N_f} E_c \left(\frac{I}{I_{c,q}(z)}\right)^{n_q(z)} \mathrm{d}z}{N_f \int \mathrm{d}z}, \tag{6}$$

where the voltage of individual filament are summed for each z-coordinate. The transition between the two limits depends on the ratio of filament resistance and matrix resistance [13, 16]. At higher voltages, the EI curves start to deviate from the power-law behaviour due to parallel Ohmic conductance, as some current starts to propagate along the matrix and the Cu shell.

A further demonstration of the model simulations and analytical limits is shown in figure 6, where curves are simulated for $\rho_m = 1 \times 10^{-8}$ Ω m with three different combinations of twist pitch L_p and bending wavelength L_w with respect to the simulated strand length L, and the peak bending strain ε_b. The limiting behaviour of the three cases is described well by (5) and (6) which are analytical equations that depend solely on the I_c and n-value distributions. The numerical solutions provide the voltage level where the transition between the two limits occurs.

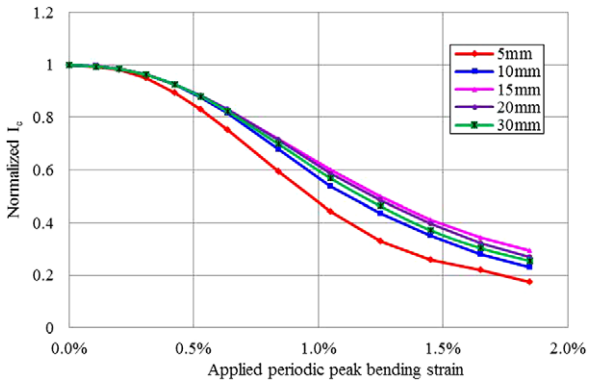

Figure 7. Normalized I_c dependence on peak bending strain for an OST1 strand with strand twist pitch of 15 mm and different bending wavelengths.

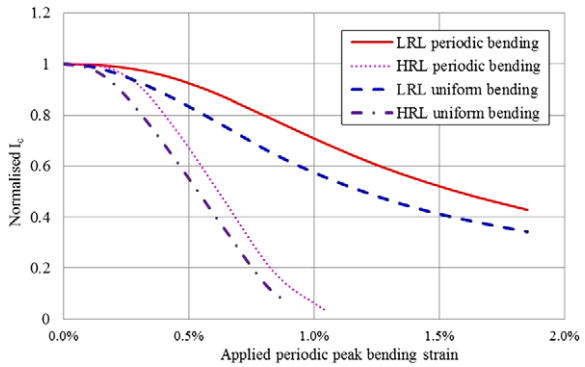

Figure 8. The HRL and LRL for the cases of uniform and periodic bending.

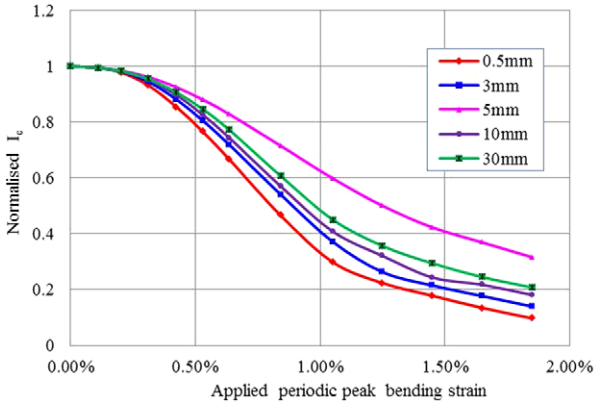

Figure 9. Normalized I_c dependence on peak bending strain for an OST1 strand with bending wavelength of 5 mm for different twist pitches.

4. Bending wavelength

The model imports the strain map from the FEM calculation, as described in section 2. The FEM calculation has been carried out explicitly for the 5 mm bending wavelength, which corresponds to the bending period used in recent TARSIS experiments. Here, we demonstrate the influence of the bending wavelength by simulating with different bending wavelengths while simply assuming that the strain waveform distribution remains the same. The validity of this assumption will be checked by performing FEM analysis for different wavelengths later on. The motivation here is comparison against the previous experimental result [2] wherein bending wavelengths of 5, 7, and 10 mm produced no significant difference in the I_c dependence with ε_b.

The filament strains are calculated from the bending waveform of the strand and the strand twist pitch, which determine the filament locations with respect to the strand neutral axis. For the filament locations, we have chosen the OST1 strand cross section (figure 3(a)) and the standard ITER twist pitch of 15 mm for this model study [26, 27]. It is an internal tin strand with a filament region that consists of 19 filament bundles. In the internal tin strands, filament bridging is a common occurrence [28] and we may assume such filament bridging occurs frequently between filaments within each filament bundle. Therefore, we consider a filament bundle as one effective filament and construct a model cross section, as shown in figure 3(b).

The simulation results in terms of normalized I_c ($I_c(\varepsilon_b)/I_{c0}$) (figure 7) show that the I_c dependence on ε_b changes with the bending wavelength, but the difference is indeed rather limited. It shows that the best performance is reached when the bending wavelength is similar to the twist pitch. The filament strain distribution is a function of both bending wavelength and strand twist pitch. The individual filament strain profile along the strand axis is determined by the strain variation due to the twisting of filament coordinates that is superimposed on the strain variation due to periodic bending. Further analysis on the combined effect on the filament strains is performed in section 5.

Figure 8 shows the LRL and HRL of uniform and periodic bending in order to explain the historical misconception from the early bending tests that most strands follow the LRL; due to the use of the Ekin uniform bending rather than the one for periodic bending. It shows that in reality most strands are in between the LRL and HRL.

5. Strand twist pitch

In this section we look at the influence of the twist pitch in relation to periodic and uniform bending. The relevant twist pitch for TARSIS testing of ITER strands is 15 mm, but it is also interesting to investigate the twist pitch dependence. For example, Muzzi *et al* [23] has experimentally shown the strong influence of strand twisting on the strain dependence of I_c in the case of uniform bending. In a twisted strand, all filaments go through the most strained region, while in an untwisted strand the filament strains remain constant, as the filament locations with respect to the neutral plane do not change and the bending profile is uniform. Although we have no such experimental data for the periodic bending case, the strand model is able to simulate strands with any twist pitch.

Figure 9 shows the results for twist pitch lengths ranging from 0.5 to 30 mm, where again the reduction of the I_c appears to be least for $L_p = 5$ mm, with the twist pitch similar to bending wavelength. An interference occurs between the selected combination of twist pitch and bending wavelength,

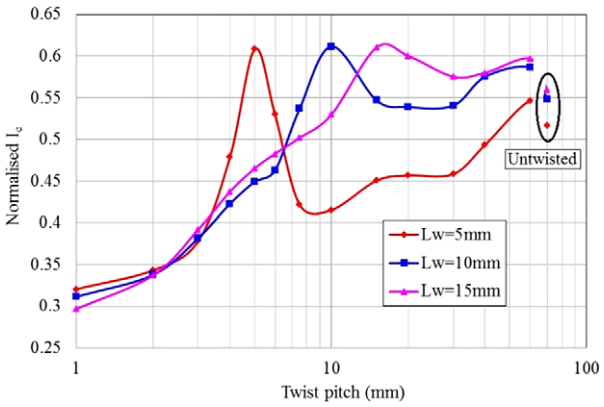

Figure 10. The normalized I_c dependence on twist pitch for an OST1 strand with different bending wavelengths under 1.05% periodic peak bending strain. The resonance peak with highest I_c occurs when the twist pitch and bending wavelength are similar.

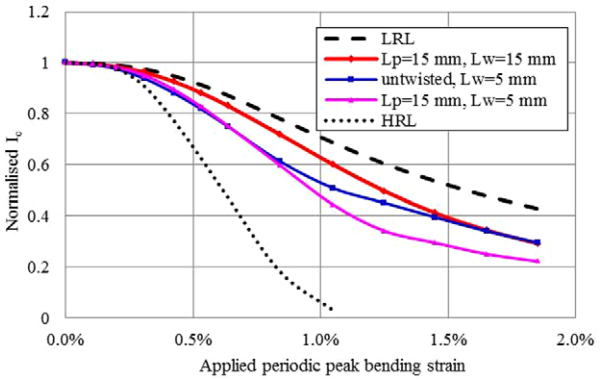

Figure 11. The normalized I_c dependence on strain for a twisted and untwisted OST1 strand under periodic bending.

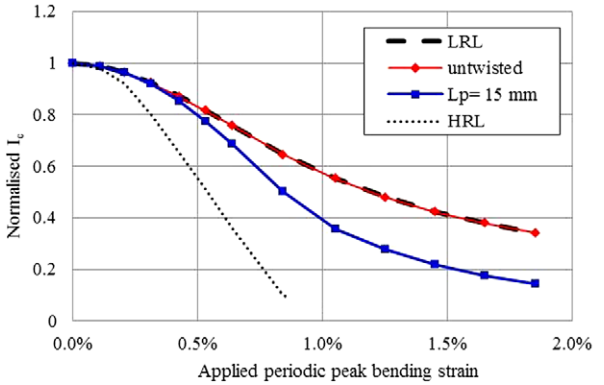

Figure 12. The normalized I_c dependence on strain for a twisted and untwisted OST1 strand under uniform bending.

leading to a resonance and stabilization towards longer twist pitch, which is illustrated in figure 10. The resonance peak with highest I_c occurs when the twist pitch and bending wavelength are similar.

The reduction of the I_c versus ε_b for various combinations of periodic and uniform bending with twist ($L_p = 15$ mm) or untwisted wires are depicted in figures 11 and 12. For

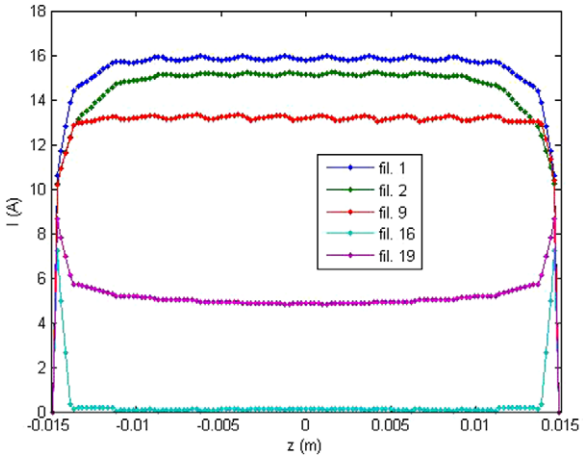

Figure 13. The current distribution in different filaments for the OST1 strand with L_w and L_p both 5 mm under 1.05% periodic peak bending strain at a critical current of 181 A. See figure 3(b) for filament position.

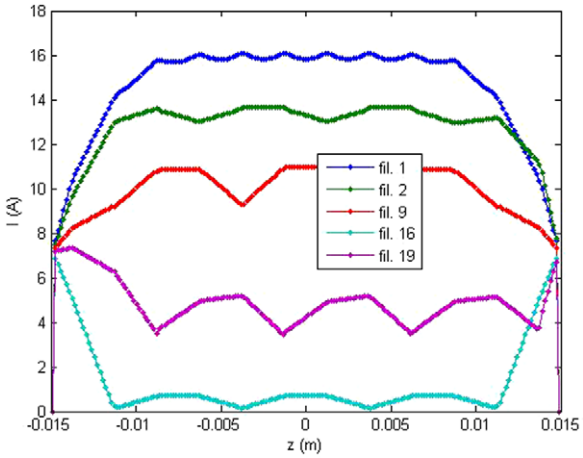

Figure 14. The current distribution in different filaments for the OST1 strand with 15 mm twist pitch and 5 mm bending wavelength under 1.05% periodic peak bending strain at a critical current of 136 A. See figure 3(b) for filament position.

periodic bending, the I_c is the highest for twist pitch similar to bending wavelength, even including the untwisted case. For uniform bending, the highest I_c is reached for untwisted wire and reaches the LRL case, as illustrated in figure 12.

Since the filament strain depends on the combined effect of the strand twist and the periodic bending, filaments with different angular position are under different periodic strain maps. Consequently, the current is distributed according to the resultant strain map, and we illustrate this effect for the case of an OST1 strand under 1.05% peak bending strain with $L_w = 5$ mm and $L_p = 5$ mm (figure 13) and with $L_w = 5$ mm and $L_p = 15$ mm (figure 14). In the figures, the currents in the filaments at the centre (fil. 1), at the first hexagonal ring (fil. 2), at the second hexagonal ring (fil. 9), and at the third hexagonal ring on opposing sides (i.e. phase shift of pi) of fil. 1 (fil. 16 and 19) are plotted. In the case when the twist pitch and the bending wavelength are similar, each filament's periodic strain variation is smaller compared to the

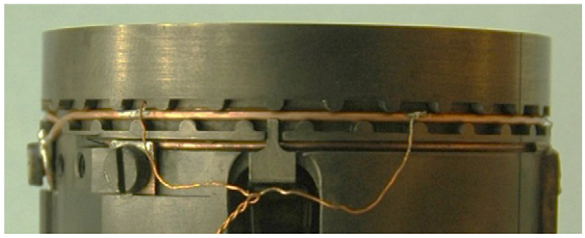

Figure 15. The position of the voltage taps in the TARSIS bending test.

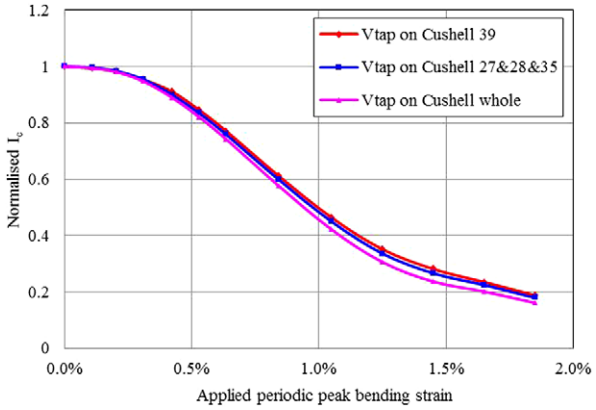

Figure 16. The position of the voltage taps has a minor influence on the result of a TARSIS test. See figure 3(b) for filament position.

case of a dissimilar twist pitch and bending wavelength. This results in less current redistribution among filaments, hence the resonance effect. This resonance peak is also reported in [29].

6. Location of voltage taps in the TARSIS bending measurement

The voltage taps in the TARSIS bending test are soldered only on the outer surface of the mounted strand, with a separation of 25 mm (see figure 15). With the strand model we investigated the influence of the radial and axial position on the shape of the *VI* transition and the normalized I_c. Figure 16 summarizes the results and shows the difference between the standard TARSIS configuration, the average and the peak value. The average potential on the surface is taken at the cross section of the wire where in the TARSIS experiment the voltage taps are attached. The greatest deviation is found on top (or beneath) the wire with wire orientation as in figure 15. At an applied peak bending strain of 1%, the difference in normalized I_c between the TARSIS configuration and the average potential is less than 5%.

7. Comparison with TARSIS measurement

The normalized I_c of the experimental TARSIS bending result, obtained on the OST1 strand with a periodic bending wavelength of 5 mm, is compared with the prediction in figure 17, together with the HRL and LRL. Taking into account that the prediction of the $I_c(\varepsilon_b)/I_{c0}$ is based only

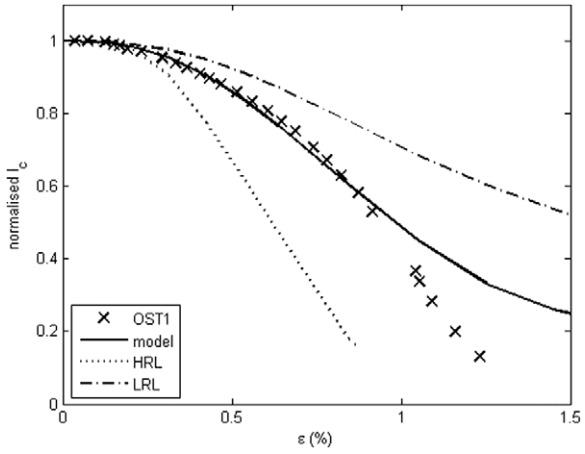

Figure 17. The normalized I_c dependence on peak bending strain ε_b from TARSIS measurements on the OST1 strand compared against simulation results ($L_w = 5$ mm) and the analytical HRL and LRL. The filament strain map distribution is taken from the FEM computations.

on the strand internal geometry, the intra-strand resistance measurements and the filament strain distribution from the FEM calculation, it can be said that the result is strikingly good. The I_c degradation with peak bending strain is in-between the LRL and HRL for periodic bending and that prediction and experimental data start to deviate at about 1% peak bending strain.

A possible explanation for the measured I_c degradation is filament fracture, which is at the moment unaccounted for in the model study presented here. The number of filament cracks observed in the TARSIS samples tested up to a peak bending force of 10 kN m^{-1} is being analysed in collaboration with the ASC group in Tallahassee. For ITER Nb_3Sn internal tin samples tested in TARSIS and afterwards analysed for filament crack distribution, it appeared that no cracks were observed when loaded up to 6 kN m^{-1}, which corresponds to a peak bending strain of just above 1% [30], according to the simplified relation from [1, 2], and a peak bending strain of about 0.8% for the FEM computation [11]. Cracks were found only in samples loaded up to 10 kN m^{-1} (peak bending strain of about 1.5% or 1.3% for FEM). It should be noted that the peak bending strain is defined as the maximum strain at the outer region of the filamentary region and most filaments are subjected to much lower strain.

As the crack analysis suggests a negligible role for filament fracture on I_c degradation below 0.8% peak bending strain, we conclude that the degradation is mainly due to strand deformation causing a strain distribution in the filaments, which is simulated well by the model.

The simulation of the *n*-value, taken from the *EI* curve between 10 and 100 μV m^{-1}, is plotted in figure 18 as a function of the bending strain. Compared to the measured data from TARSIS. The match is not as good as in the case of I_c, however, considering the complexity of the strand internal structures and variations in the strand transport properties, the model demonstrates its ability to predict both I_c and *n*-value rather well.

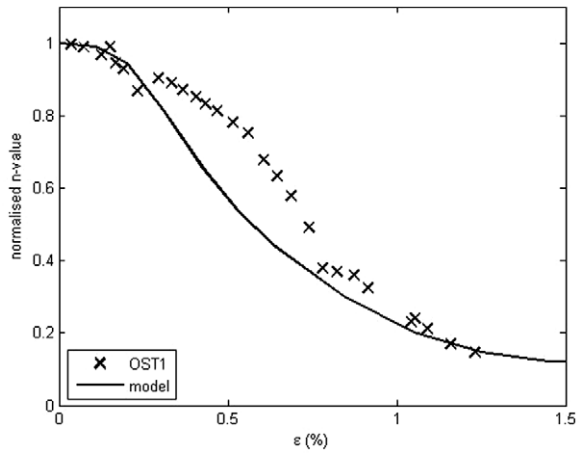

Figure 18. The normalized n-value dependence on peak bending strain ε_b from TARSIS measurements on the OST1 strand compared against simulation results ($L_w = 5$ mm). The filament strain map distribution is taken from the FEM computations.

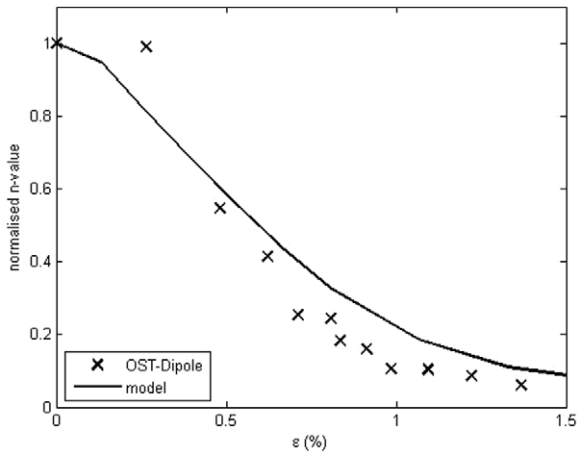

Figure 20. The normalized n-value dependence on peak bending strain ε_b from TARSIS measurements on the OST-dipole RRP strand compared against simulation results ($L_w = 5$ mm). The filament strain map distribution is taken from the FEM computations.

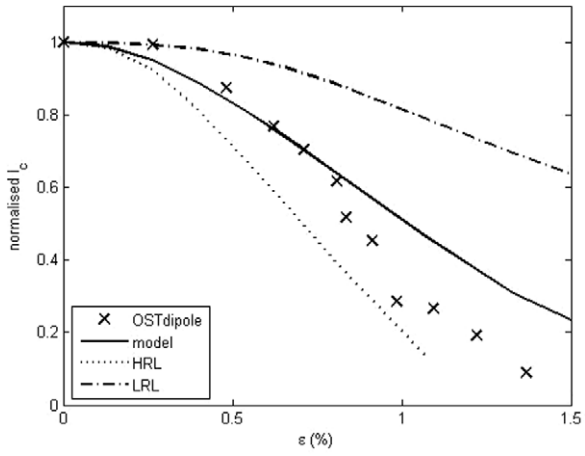

Figure 19. The normalized I_c dependence on peak bending strain ε_b from TARSIS measurements on the OST-dipole RRP strand compared against simulation results ($L_w = 5$ mm) and the analytical HRL and LRL. The filament strain map distribution is taken from the FEM computations.

The experimental data from another strand, the OST-dipole RRP type [31, 32], are compared to the model simulations in figure 19, for the normalized I_c, and in figure 20, for the normalized n-value. The experimental I_c starts to deviate from the predicted values after 0.7% strain. Tensile stress–strain tests on this wire showed that the wire collapses around 0.6% strain, so around this level the influence of cracks may be expected. At low values of applied strain, both experimentally determined I_c and n-value remain higher than the predicted values. Altogether we find a good agreement between prediction and experiment in OST1 (internal tin) and OST-dipole (restacked-rod process) wires, there is still around 10% deviation in bronze-type wires. We believe that implementing the diffusion barrier in the strand model may improve the outcome for the *EI* transition at higher E levels, which may tweak the prediction of the n-value as well. In addition, improved mechanical modelling of the strand (plastic) deformation may also help to achieve an even better result in quantitative terms.

8. Conclusions

We developed a novel numerical strand model constructed as a 3D network of resistors including superconducting filaments, normal matrix elements, and an outer stabilizing shell or inner core. The model accurately simulates the voltage–current characteristic in a periodic bending experiment and provides the associated spatial potential distribution. The current–voltage characteristics representing the low- and high-resistivity limits (LRL and HRL) were identified for periodic and uniform axial bending. Various influences due to combinations of twist pitch and bending periodicity have been discussed and the influence of the position of the voltage taps has been investigated.

The simulation results are compared against I_c reduction, as experimentally measured by the TARSIS facility, versus the assessed peak bending strain and show a good agreement.

References

[1] Nijhuis A, van den Eijnden N C, Ilyin Y, van Putten E G, Veening G J T, Wessel W A J, den Ouden A and ten Kate H H J 2005 Impact of spatial periodic bending and load cycling on the critical current of a Nb_3Sn strand *Supercond. Sci. Technol.* **18** S273–83

[2] Nijhuis A, Ilyin Y, Wessel W A J and Abbas W 2006 Critical current and strand stiffness of three types of Nb_3Sn strand subjected to spatial periodic bending *Supercond. Sci. Technol.* **19** 1136–45

[3] Nijhuis A, Ilyin Y, Wessel S, Krooshoop E, Feng L and Miyoshi Y 2009 Summary of ITER TF Nb_3Sn strand testing under axial strain, spatial periodic bending, and contact stress *IEEE Trans. Appl. Supercond.* **19** 1516–20

[4] Nunoya Y, Isono T and Okuno K 2004 Experimental investigation on the effect of transverse electromagnetic force on the V–T curve of the CIC conductor *IEEE Trans. Appl. Supercond.* **14** 1468–72

[5] Mitchell N 2002 Analysis of the effect of Nb_3Sn strand bending on CICC superconductor performance *Cryogenics* **42** 311–25

[6] Mitchell N 2008 Comparison between predictions and measurements of the superconducting performance of Nb_3Sn cable in conduit conductors with transverse load degradation *Supercond. Sci. Technol.* **21** 054005

[7] Koizumi Y, Nunoya Y and Okuno K 2006 A new model to simulate critical current degradation of a large CICC by taking into account strand bending *IEEE Trans. Appl. Supercond.* **16** 831–4

[8] Murakami H, Ishiyama A, Ueda H, Koizumi N and Okuno K 2007 Numerical simulation of critical current and *n*-value in Nb_3Sn strand subjected to bending strain *IEEE Trans. Appl. Supercond.* **18** 1394–7

[9] Zignani C F, Corato V, Muzzi L and della Corte A 2010 Numerical simulation of Nb_3Sn strands performances with bending strain and comparison with experimental measurements *IEEE Trans. Appl. Supercond.* **20** 1432–5

[10] van Lanen E P A and Nijhuis A 2010 JackPot: a novel model to study the influence of current non-uniformity and cabling patterns in cable-in-conduit conductors *Cryogenics* **50** 139–48

[11] Bajas H, Durville D, Ciazynski D and Devred A 2010 Numerical simulation of the mechanical behavior of ITER cable-in-conduit conductors *IEEE Trans. Appl. Supercond.* **20** 1467–70

[12] Warnes W H and Larbalestier D C 1986 Critical current distributions in superconducting composites *Cryogenics* **26** 643–53

[13] Plummer C J G and Evetts J E 1987 Dependence of the shape of the resistive transition on composite inhomogeneity in multifilamentary wires *IEEE Trans. Magn.* **23** 1179–82

[14] Hampshire D P and Jones H 1987 Analysis of the general structure of the *E–I* characteristic of high current superconductors with particular reference to a Nb-Ti SRM wire *Cryogenics* **27** 608–16

[15] Ekin J W 1980 Strain scaling law and the prediction of uniaxial and bending strain effects in multifilamentary superconductors *Proc. Topical Conf. on A15 Superconductors* pp 187–203

[16] Ciazynski D and Torre A 2010 Analytical formulae for computing the critical current of an Nb_3Sn strand under bending *Supercond. Sci. Technol.* **23** 125005

[17] Miyoshi Y, van Lanen E P A, Dhallé M M J and Nijhuis A 2010 Microscopic fractures and transport degradation in ITER type Nb_3Sn strands *IEEE Trans. Appl. Supercond.* **20** 1404–7

[18] Lucas E J, Stekly Z J J, Laverick C and Pewitt G 1965 Current transfer in contacts involving superconductors *Int. Adv. Cryog. Eng.* **10** 113–23

[19] Bottura L and Bordini B 2009 $J_c(B, T, \varepsilon)$ parameterization for the ITER Nb_3Sn production *IEEE Trans. Appl. Supercond.* **19** 1521–4

[20] Zhou C, van Lanen E P A, Veldhuis D, ten Kate H H J, Dhallé M and Nijhuis A 2011 Direct measurement of inter-filament resistance in superconducting multifilamentary NbTi and Nb_3Sn strands *IEEE Trans. Appl. Supercond.* **21** 2501–4

[21] Zhou C, Miyoshi Y, van Lanen E P A, Dhallé M M J and Nijhuis A 2012 Direct measurement of inter-filament resistance in various multi-filamentary superconducting NbTi and Nb_3Sn strands *Supercond. Sci. Technol.* **25** 015013

[22] Corato V, Muzzi L, Bessi Vetrella U and della Corte A 2009 Direct measurement of interfilament resistance in Nb_3Sn strands *J. Appl. Phys.* **105** 093930

[23] Muzzi L, Corato V, Viola R and della Corte A 2008 Performance enhancement under bending of Nb_3Sn strands with untwisted filaments *J. Appl. Phys.* **103** 073915

[24] Koizumi N, Murakami H, Hemmi T and Nakajima H 2011 Analytical model of the critical current of a bend Nb_3Sn strand *Supercond. Sci. Technol.* **24** 055009

[25] Godeke A, Dhalle M, Morelli A, Stobbelaar L, van Weeren H, van Eck H J N, Abbas W, Nijhuis A, den Ouden A and ten Haken B 2004 A device to investigate the axial strain dependence of the critical current density in superconductors *Rev. Sci. Instrum.* **75** 5112–8

[26] Vostner A and Salpietro E 2006 Enhanced critical current densities in Nb_3Sn superconductors for large magnets *Supercond. Sci. Technol.* **19** S90–5

[27] Nijhuis A 2008 A solution for transverse load degradation in ITER Nb_3Sn CICCs: verification of cabling effect on Lorentz force response *Supercond. Sci. Technol.* **21** 054011

[28] Ghosh A K, Robins K E and Sampson W B 1985 *IEEE Trans. Magn.* **21** 328–31

[29] Murakami H, Ueda H, Ishiyama A, Koizumi N and Okuno K 2008 Numerical simulation of critical current performance in Nb_3Sn strand subjected to periodic bending deformation *Denki Gakkai Ronbunshi* **6** 853–9

[30] Sanabria C *et al* 2011 Metallographic examination of filament fracture in ITER Nb3Sn TF strands after transverse and axial loading tests *CEC-ICMC Cryogenic Engineering Conf. & Int. Cryogenic Materials Conf. (Spokane, WA, June 2011)*

[31] Nijhuis A, Ilyin Y and Abbas W 2008 Axial and transverse stress–strain characterization of the EU dipole high current density Nb_3Sn strand *Supercond. Sci. Technol.* **21** 065001

[32] Vostner A *et al* 2008 Development of the EFDA dipole high field conductor *IEEE Trans. Appl. Supercond.* **18** 544–7